Impact of graphite foil rolling on the thermal field homogeneity of spark plasma sintering

Joseph Le Cloarec, Sylvain Marinel, Geoffroy Chevallier, Claude Estournès, Charles Manière

Impact of graphite foil rolling on the thermal field homogeneity of spark plasma sintering

Joseph Le Cloarec[1,2]*, Sylvain Marinel[1], Geoffroy Chevallier[2], Claude Estournès[2], Charles Manière[1]*

1. CRISMAT, Normandie Univ, ENSICAEN, UNICAEN, CNRS, 14000, Caen, France
2. CIRIMAT, Université de Toulouse, CNRS, INPT, UPS, 31062 Toulouse, France

Keywords

Spark Plasma Sintering; Field Assisted Sintering Technique; contact resistance; simulation; graphite foil;

Abstract: Heating and thermal gradients are important parameters in Spark Plasma Sintering (SPS) affecting densification, structure and microstructure of materials. Controlling those parameters requires advanced Joule heating simulations. The key aspect of these models is the identification of the electrical and thermal contact resistances (ECR and TCR) in the SPS tooling. The latter have a high importance to explain the experimental temperature field. The ECRs and TCRs have already been determinated in a previous work by simulating the experimental thermal field. However, these previous studies consider rolled graphite foil placed between the die and punches. ECRs and TCRs have been recalibrated to consider a "no rolling graphite foil", using SPS experiments equipped with several temperature measurements points. Those new tests shows that the previous model overestimated the temperature of the punches and sample up to 400°C when applied to a configuration with "no rolling graphite foil". This recalibration also demonstrates it is necessary to divide the foil ECR by 2 and the TCR by 10 to obtain a predictive simulation of the thermal field. This study also shows that the use of a "no rolling graphite foil" reduces significantly the heterogeneity of thermal field.

Graphical Abstract

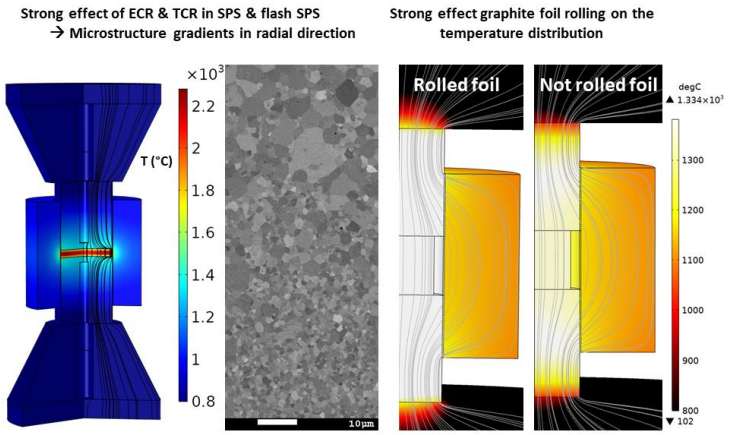

* Corresponding author:
Laboratoire de cristallographie et sciences des matériaux (CRISMAT)
6 Bvd du maréchal Juin 14050 CAEN CEDEX 4, France
E-mail address: joseph.le-cloarec@ensicaen.fr; charles.maniere@ensicaen.fr

1. Introduction

Spark Plasma Sintering is a sintering process combining die pressing generally in graphite tools and a pulsed current Joule heating. The heating is mostly hybrid as the electrical current passes through the powder and the graphite tools depending on the powder conductivity. The high temperatures (>2000 °C) combined with the high pressures (~100 MPa) allow the sintering of materials that are very difficult to process by free-sintering such as Ultra-High-Temperature-Ceramics [1–3], Functionally Graded Material [4–6], refractory metals [7–9] . They also permit to obtain microstructures with interesting properties [10–12] in shorter times compared to Hot Pressing or Hot Isostatic Pressing.

Temperature control is mandatory for the mastery of the SPS process. A careful management of the graphite pressing column geometry is required to homogenize the thermal field [13–15]. Thermal contact resistances (TCR) and electrical contact resistances (ECR) between the pressing parts play an important role in the distribution of heat within the tooling [16–18]. The TCR increase the temperature difference between the parts and tend to confine the heat in the powder [19,20]. This effect is particularly important in Flash-SPS [21–23]. The ECR increase the electrical power dissipation at the interface making the SPS process more energy efficient [15,24,25]. The ECR and TCR have a strong impact in the underestimation of the sample temperature and the thermal field distribution.

For a better understanding and control of the mechanisms involved in SPS, several authors have simulated the Joule heating by the Finite Element Method (FEM) with a focus on TCR and ECR [13,16,19,26–31]. The contact resistances decrease with the temperature and the applied pressure [19,32,33]. The dependence of ECR and TCR with temperature and pressure is difficult to determine by direct measurements. Most authors calibrate them by comparing the simulated and experimental thermal fields [19,30,34]. The contact resistance of the punch/die interface is particularly important. It is difficult to estimate because it depends on the gap between the die and the punch and on the behavior of the graphite foil generally present at this

interface. In this particular interface, the contact pressure is very low. It results from the difference in thermal expansion between the die and the piston. The mechanical strength of the graphite sheet also influences this pressure. [17,19,30]. This parameter can be determined empirically for obtaining functional models but these models are limited rest to their specific experimental conditions (temperature, pressure, tooling size [19,30]). Moreover, these models do not take into account the various possible treatments undergone by the graphite foil. For example rolling has an important influence on the distribution of the thermal field in the SPS tooling. In this paper, the term "rolled graphite foil" refers to a graphite foil that has been passed through a rolling mill prior the punch die assembly.

A rolled graphite foil increase the thermal heterogeneity between punches and die while a "no rolling graphite foil" reduce those temperature differences. The figure 1.a shows the temperature differences between the punch and die as a function of die temperature in two conductive SPS experimental configuration, one with a "no rolling graphite foil" and the other with a rolled graphite foil. The temperature difference in the SPS tooling at 925°C (die temperature) is 250°C in the use of a rolled graphite foil while it is only 100°C with a "no rolling graphite foil". Those experiments also shows that in the case of rolled graphite foil the thermal ripple due to PID regulation is undergone by the punches and sample while it is not seen on temperature control (die temperature). This experiment constitute an experimental evidence of the effect of graphite foil rolling on thermal field homogeneity in SPS tooling. To the best of our knowledge, this effect has not already been studied in literature and deserves to be carefully identified since it may have important effect on the properties of the sintered material. In the case study of flash SPS reported in figure 1.b [10.1016/j.jeurceramsoc.2021.09.021], a high thermal confinement result the TCR and low heating times. In addition, an important microstructure gradient develops in the zirconia specimen.

The present article reports the "no rolling graphite foil" properties identified by the experimental exploration of the thermal field and the correction of the previous ECR/TCR model proposed by C. Manière et al.[19] on rolled graphite foils.

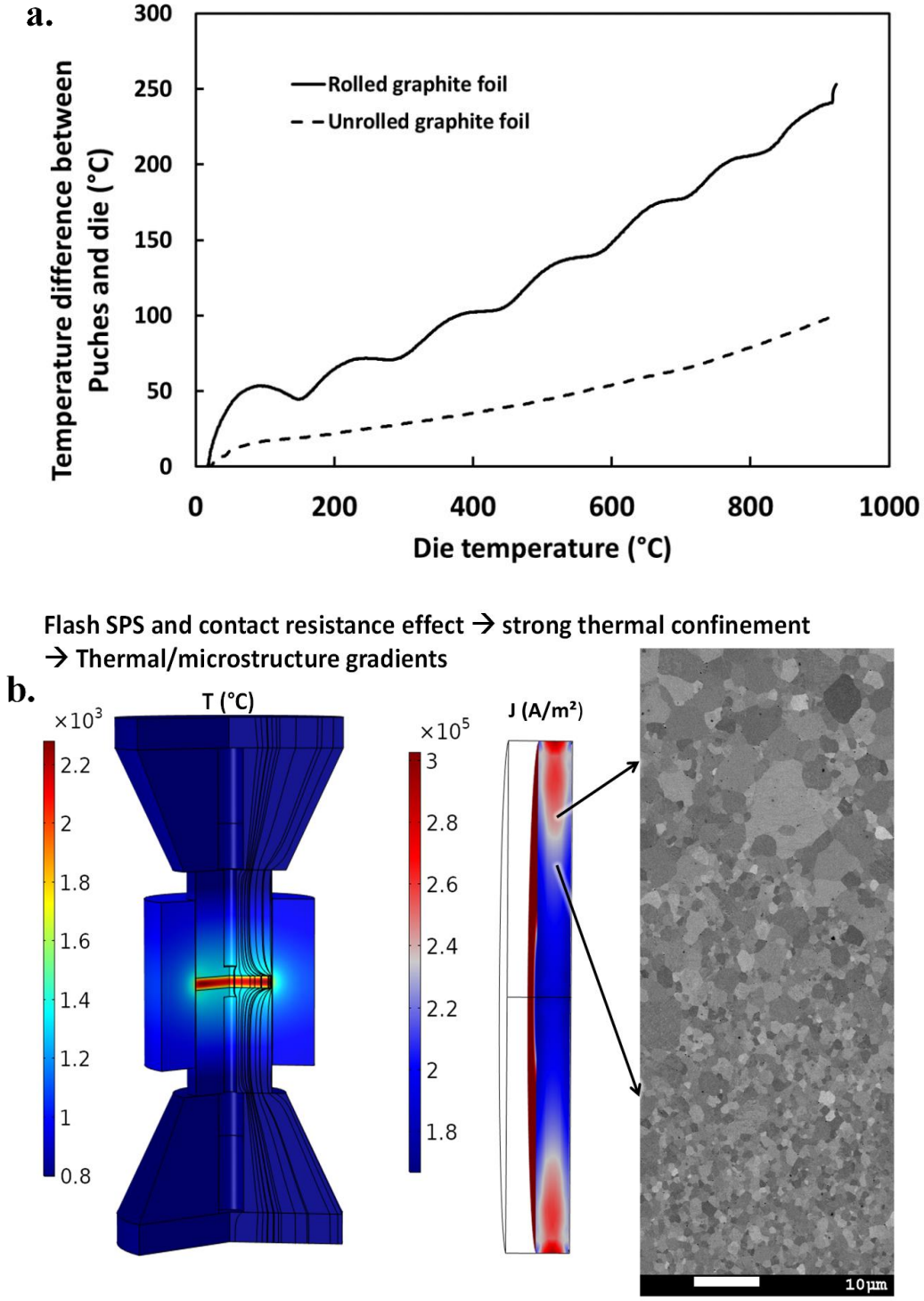

Figure 1 a. The evolution of temperature difference between punches and die as a function of the die temperature in SPS experiments using a "no rolling" and a rolled graphite foil. b. application example of flash SPS of a 30 mm zirconia specimen where the TCR implies a high thermal confinement and the development of microstructural gradient.

2. Experiment and method

2.1. Experimental configuration

Experiments were performed with the SPS machine Dr. Sinter 2080 (Japan) of the Plateforme Nationale CNRS de Frittage Flash (PNF2) located at the Université Toulouse 3 Paul Sabatier. Toyo Tanso© provided the graphite grade ISO68 used for the dies, spacers, punches and sample. In all experiments, a not-rolled 200 µm thick graphite foil (PERMA FOIL®Toyo Tanso) was applied to cover the inner wall of the die and the interfaces punch/powder and spacer/electrode.

Rolled graphite foils are thinned by passing through rolling mill, they do not undergo any other modification. Rolling graphite foil or not is a habit specific to SPS users. The main purpose of this rolling step is to facilitate the insertion of the graphite foil inside the die and then the puncher within the graphite foil. This rolling step is not necessary for a correct assembly so all SPS users do not practice it.

Experiments were performed with a graphite pellet and in the configuration shown in Figure 2. In one experiment, the graphite foils between the sample and the punch were not covered with BN allowing the conduction of current through the sample. In another experiment, the graphite foils were covered with BN (boron nitride), which prevent the current to flow through the sample. These configurations are further referred as “conductive” and “insulated”. The control temperature governing the current flow through the column was measured at the red point shown in Figure 2 (Tcontrol), at 3 mm from the die surface. Other temperatures were measured (using a Graphtec controller) at points T1, T2 and T3 in order to map the thermal field during the experiment. The die has been heated up from 35°C to 1100°C in 700s under an uniaxial pressure of 50 MPa on punchers. After reaching the temperature of 1100°C, the current is cut off for cooling and the pressure is released.

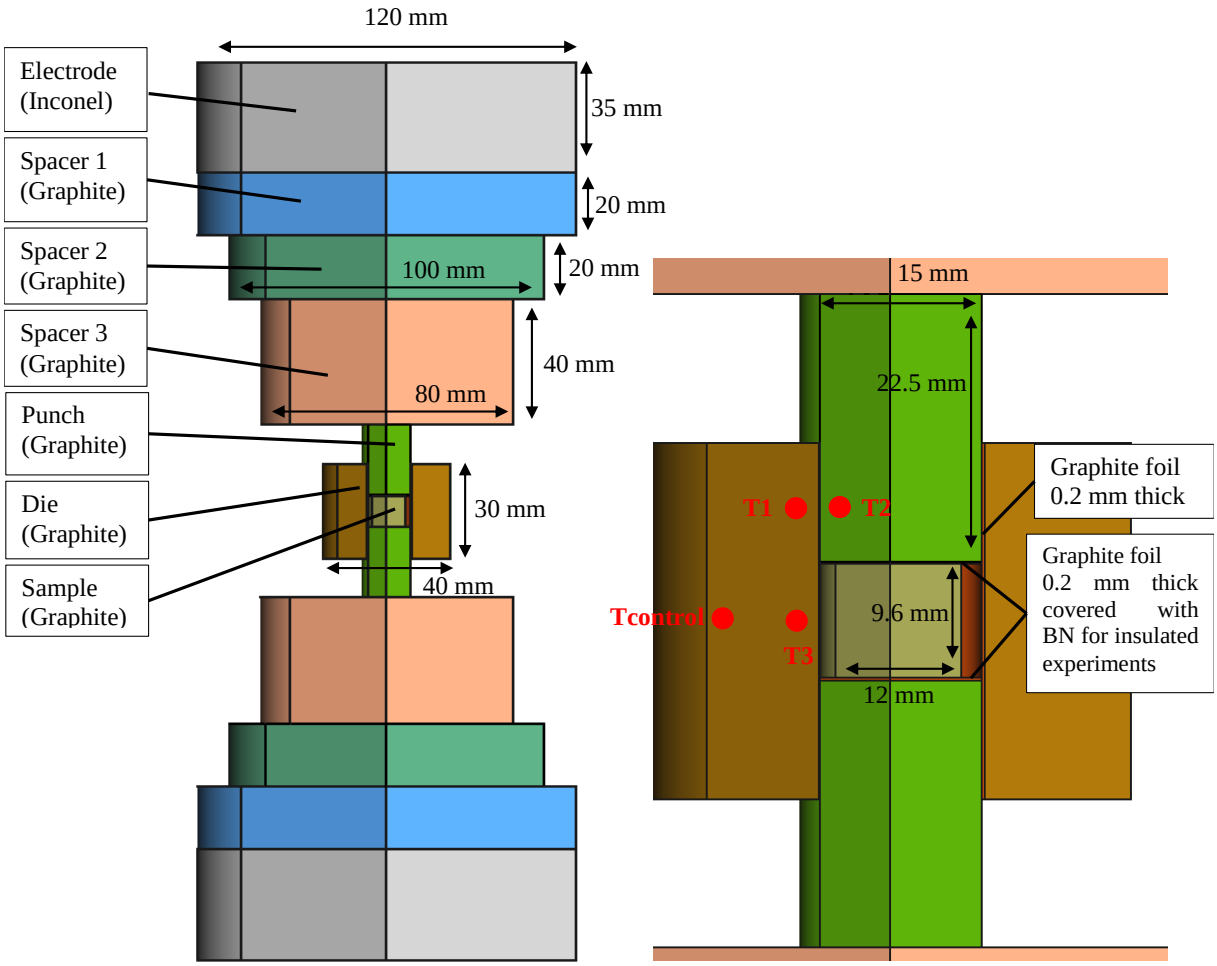

Figure 2 SPS column dimension and setup for experiments.

The simulation uses the software Comsol Multiphysics® and the same configuration as for the experiments and the same model as in the previous study by C. Manière et al [19].

2.2. Calculation

The Joule heating model obeys the current Eq. (1) and the heat Eq (2) :

$$\nabla \bullet \vec{j} = \nabla \bullet \left(\sigma \vec{E}\right) = 0 \qquad (1)$$

$$\nabla \bullet (-\kappa \nabla T) + \rho C_p \frac{\partial T}{\partial t} = \mathrm{JE} \qquad (2)$$

With $\vec{j}$ the current density (A.m^{-2}), σ the electrical conductivity (Ω^{-1}.m^{-1}), T the temperature (K), E the electric field (V.m^{-1}).

The thermal model uses two main boundary conditions. Surface radiation is modeled by the surface to surface radiation implemented in the heat transfer module of Comsol Multiphysics® and is described in [www.comsol.com].

The water cooling system heat flux is modeled by the following convective flux Eq. (3):

$$\emptyset_c = \mathrm{h}_c(T_{electrode} - T_{water}) \quad (3)$$

With $\emptyset_c$ the conductive heat flux ($W.m^{-2}$), h_c the convective coefficient ($W.m^{-2}.K^{-1}$), $T_{electrode}$ and T_{water} respectively the temperature of the electrode (K) and the temperature of water (K).

The electrical and thermal contact conditions at the inner interfaces obey Eqs. (4) and (5):

$$J_c = \frac{1}{ECR}(U_1 - U_2) \quad (4)$$

$$\dot{q}_c = \frac{1}{TCR}(T_1 - T_2) \quad (5)$$

With J_c the contact current density ($A.m^{-2}$), U_1 and U_2 the tension on both sides of the interfaces (V), $\dot{q}_c$ the contact heat flux ($W.\ m^{-2}$), T_1 and T_2 the temperature on both sides of the interfaces (K).

The TCR and ECR, electrode/spacer1, spacer1/spacer2 and spacer2/spacer3 are modeled by a pressure dependent behavior. Since these contacts are far away the heating zone, temperature has an negligible effect on them [19], the graphite/graphite contact resistances obey:

$$TCR_{(\frac{m^2K}{W})} = -2.09.10^{-6} \times P_{(MPa)} + 4.81.10^{-5} \quad (6)$$

$$ECR_{(\Omega m^2)} = -2.09.10^{-10} \times P_{(MPa)} + 4.81.10^{-9} \quad (7)$$

For the electrode/graphite contacts resistances, the following equations are considered:

$$TCR_{(\frac{m^2K}{W})} = -3.70.10^{-5} \times P_{(MPa)} + 1.45.10^{-3} \quad (8)$$

$$ECR_{(\Omega m^2)} = -3.70.10^{-9} \times P_{(MPa)} + 1.45.10^{-7} \quad (9).$$

The interfaces between the spacer 3, the punches, the die and the sample undergo important temperature variations. The corresponding ECR and TCR are therefore temperature dependent and obey the equations (10) and (11) under 50 MPa:

$$TCR_{(\frac{m^2K}{W})} = 5.10^{-6} + 3.10^{-5}\frac{2000-T_{(K)}}{T_{(K)}-80} \quad (10)$$

$$ECR_{(\Omega m^2)} = 5.10^{-9}\frac{2000-T_{(K)}}{T_{(K)}-80} \quad (11)$$

For the insulated experiment, the interface between the sample and the punchers are considered as fully electrically insulated.

The interface between the die and the punch is more complex. In this graphite/foil/graphite vertical contact, the heat generated tends to accumulate in the graphite foil due to the TCR on both side of the foil. Moreover, the strong thermal anisotropy of the foil need to be considered. In a previous work [19] this contact is modeled in the following way.

The punch/die ECR is modeled by an electrically resistive thickness of 0.2mm (graphite foil thickness) with anisotropic conductivity (ρ_e) along the diametrical (x) and longitudinal (y) axis. The conductivity of the foil obeys the following equations:

$$\rho_{ey\,(\Omega m)} = \rho_{egraphite\,(\Omega m)} \quad (12)$$

$$\rho_{ex\,(\Omega m)} = (-9.5.10^{-7} \times T_{(K)} + 1.7.10^{-3}) \times F_e \quad (13)$$

$$F_{e_{(no\ units)}} = 4.5.10^{-2} \times D_{(mm)} - 3.67.10^{-1} \quad (14)$$

With F_e, a scaling factor depending on the punch diameter D (mm).

On the other hand, the punch/die TCR is modeled by a thermally resistive thickness of 0.2mm with an anisotropic thermal conductivity (κ). This thickness is surrounded by two TCRs (ρ_T) at the punch/foil and foil/die contacts. This way the heat trapped in the foil can be simulated. Those thermal resistivities are:

$$TCR_{punch/die\,(\frac{m^2K}{W})} = 2 \times \left(\frac{t_{gf}}{2} \times \rho_T\right) + \frac{t_{gf}}{\kappa_x} \quad (15)$$

$$\rho_{T\,(\frac{mK}{W})} = (80 + 50\frac{2000-T_{(K)}}{T_{(K)}-80}) \times F_T \quad (16)$$

$$\kappa_{x\left(\frac{W}{mK}\right)} = \kappa_{graphite\left(\frac{W}{mK}\right)} \quad (17)$$

$$\kappa_{y\left(\frac{W}{mK}\right)} = 1230 - 6.99.10^{-2} \times T_{(K)} + 1.55.10^{-5} \times T_{(K)}^{2} \quad (18)$$

$$F_{T\,(no\ units)} = 3.11.10^{-2} \times e^{(1.15.10^{-1} \times D_{(mm)})} \quad (19)$$

With F_T, a scaling factor depending on the diameter (D) of punches and t_{fg}, the graphite foils thickness.

2.3. Material properties

All the material proprieties required are given in the following table:

Material	Heat Capacity Cp ($\frac{J}{kg.K}$)	Thermal conductivity κ ($\frac{W}{m.K}$)	Electrical resistivity ρ_e (Ω.m)	Volumic mass ρ ($\frac{kg}{m^3}$)
Inconel	$2.50.10^{-1}.T_{(K)} + 344$	$1.57.10^{-2}.T_{(K)} + 10,1$	$1.6.10^{-10}.T_{(K)} + 9,82.10^{-7}$	8430
Graphite	$-9.60.10^{-4}.T_{(k)}^{2} + 2.72.T_{(K)} + 34.27$	$1.55.10^{-5}.T_{(k)}^{2} + 6.99.10^{-2}.T_{(K)} + 123$	$-2.44.10^{-15}.T_{(k)}^{3} + 1.26.10^{-11}.T_{(k)}^{2} - 1.87.10^{-8}.T_{(K)} + 1.70.10^{-5}$	$-1.4.10^{-2}.T_{(K)} + 1904$
Not-rolled graphite foil	*Same as graphite*	κ_x = Same as graphite $\kappa_y = 1230 - 6.99.10^{-2} \times T + 1.55.10^{-5} \times T^2$	ρ_{ey} = *Same as graphite* $\rho_{ex} = (-9.5.10^{-7} \times T_{(K)} + 1.7.10^{-3}) \times F_e$	*Same as graphite*

Table 1: Graphite , graphite foil and Inconel electro-thermal properties [19]

3. Results and discussions

3.1. Effect of graphite foil rolling on thermal distribution

Previously described contact resistance model based on rolled graphite foil is applied in figure 3 to the “conductive” and “insulated” experiments with a “no rolling graphite foil”. The resulting simulation shows a mismatch between simulated and experimental temperatures. The T1, T2 and T3 simulated values are hotter than the T1, T2 and T3 measured experimental ones. The simulated and experimental Tcontrol match because this temperature is numerically PID regulated.

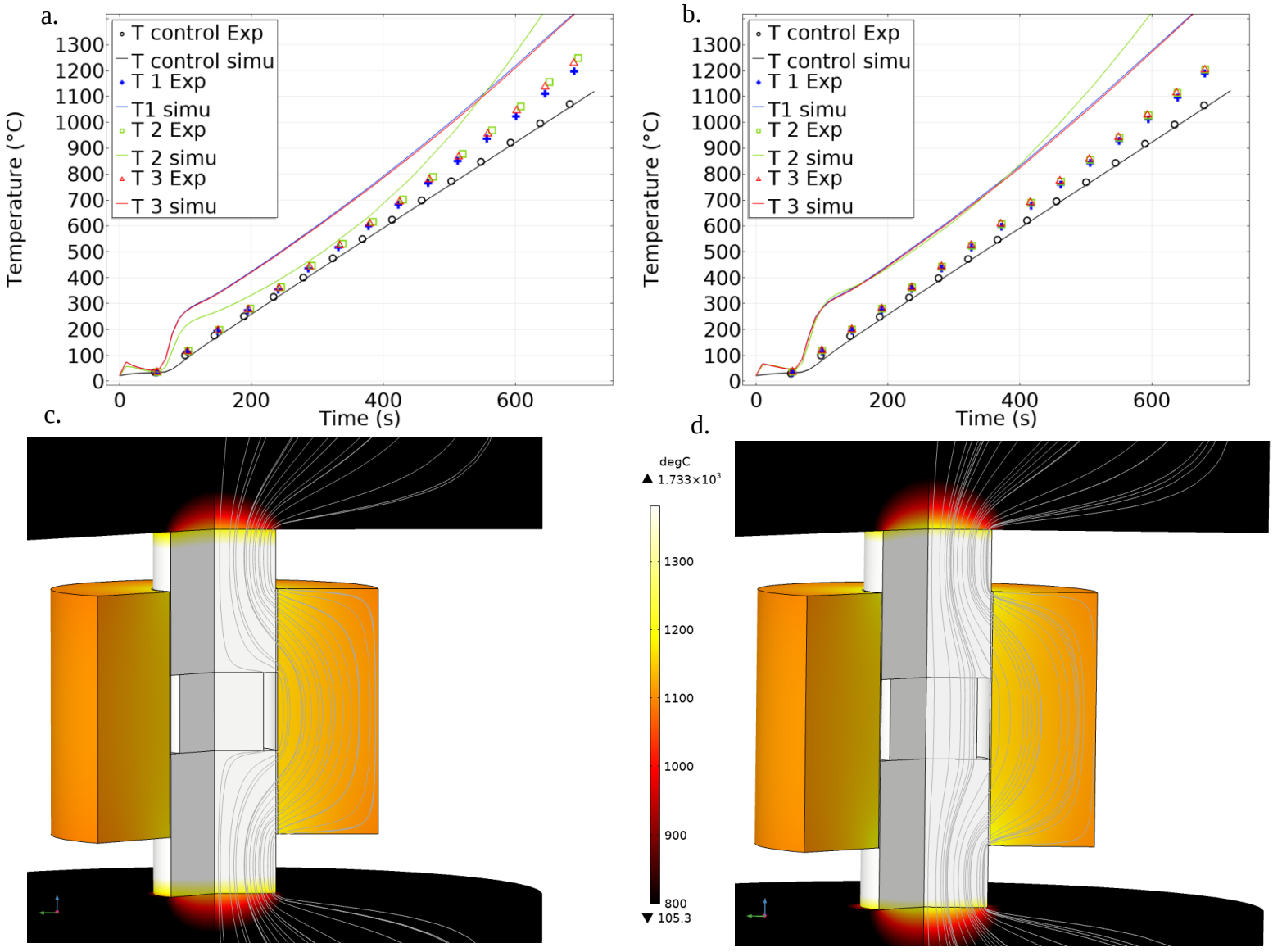

Figure 3 Simulation and experimental comparison: results of simulation realized with a model developed considering a rolled graphite foil and experiments performed with a “no rolling graphite foil”: (a) *Experimental and simulated temperatures from the insulated experiment,* (b) *Experimental and simulated temperatures from the conductive experiment, (c) Simulated*

temperature repartition from the insulated experiment, (d) Simulated temperature repartition from the conductive experiment
"T exp" refers to experimental temperatures and "T simu" refers to simulated temperatures.

This temperature difference is due to the rolling of the graphite sheet. Since the rolled graphite sheet is thinner, the effective contact area between the punches, the graphite foil and the die is lower than that of the "no rolling graphite foil". This weaker contact leads to a lower electrical and thermal conduction between the punches, graphite foil and die that is cooled by radiation. This phenomenon results in a high TCR and ECR. As the figure 3 shows the latter effect increases the temperatures differences. Rolling the graphite foil can lead to a 400K difference between experimental ("no rolling graphite foil") and simulated (rolled graphite foil) temperature. This phenomenon is the cause of a great inhomogeneity in the tooling temperature if a rolled graphite foil is used during SPS.

3.2. Model recalibration

In order to obtain a simulation closer to reality when using a "no rolling graphite foil", a correction factor is applied on the thermal and electrical resistivity of the graphite foil. F_{ce} and F_{cT} refer to the electrical and thermal corrective factor, respectively. These corrective factors allow switching from the rolled contact resistances (value of 1) to not-rolled foil case. They consider the phenomenon of lower effective contact area previously detailed but also the possible modification of thermos-electrical properties modification of graphite foil after rolling. These factors are applied to the thermal and electrical conductivity of the interface of interest.

$$\rho_{ex\,(\Omega m^2)} = (-9.5.10^{-7} \times T_{(K)} + 1.7.10^{-3}) \times F_e \times \boldsymbol{F_{ce}} \quad (20)$$

$$\rho_{T\,(\frac{mK}{W})} = (80 + 50.\frac{2000-T_{(K)}}{T_{(K)}-80}) \times F_T \times \boldsymbol{F_{cT}} \quad (21)$$

Several simulations have allowed to calibrate the values of these corrective factors. They has been modified until the simulated temperatures fit the experimental temperatures measured in

several points of the SPS tooling for both insulated and conductive experiment. For the two experiments ("isolated" and "conductive") the correction coefficient of unlaminated foil are F_{cT} = 0.1 and F_{ce} = 0.5.

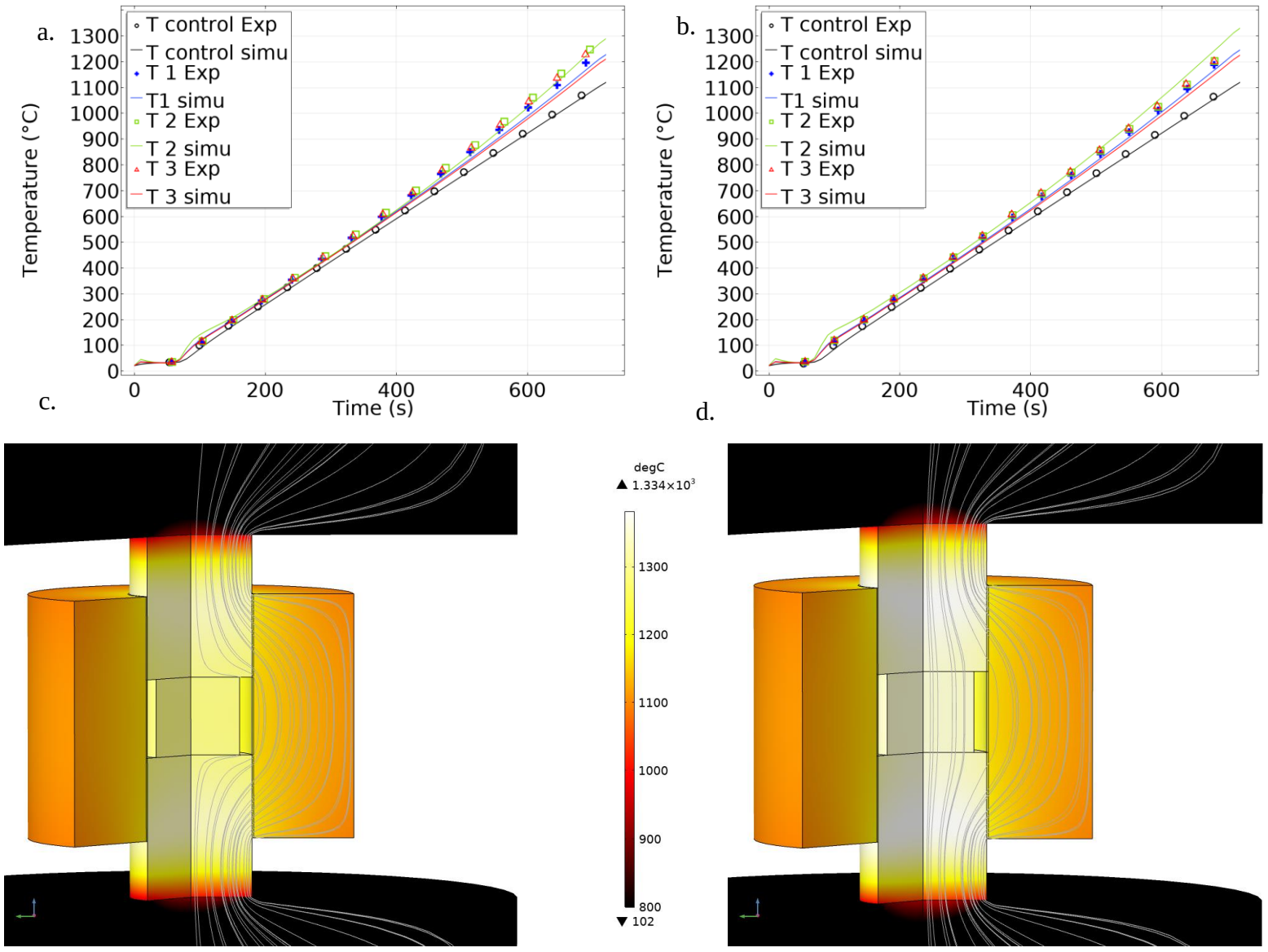

Figure 4 Simulation and experimental comparison: results of simulation realized with a model developed considering a rolled graphite foil with correctives factors (F_{cT} = 0.1 ; F_{ce} = 0.5) applied and experiments performed with a "no rolling graphite foil": (a) Experimental and simulated temperatures from the insulated experiment, (b) Experimental and simulated temperatures from the conductive experiment, (c) Simulated temperature repartition from the insulated experiment, (d) Simulated temperature repartition from the conductive experiment. "T exp" refers to experimental temperatures and "T simu" refers to simulated temperatures.

As shown on the figure 4, with the use of the two corrective factors, the simulated temperature match with the experimental temperatures. Comparing the heating behavior of

rolled foil (figure 3) and not-rolled foil (figure 4), the thermal field between the punches and die is more homogeneously distributed for the not-rolled case explored in the present work.

4. Conclusion

In this study, two SPS experiments were performed with several temperature measurement points in the tooling, one with a conductive sample and the other with an insulated sample. A simulation model was used to calibrate the electric and thermal contacts by matching the temperature field of these two experiments. The punch/die interface has a great importance on the heat distribution in the SPS tooling. The main objective of this work was to adapt the previously developed contact model to the case of “no rolling graphite foil”. This study shows the rolling of the graphite foil that ease the experiment preparation implies high thermal inhomogeneity between the parts of about 400K. The use of “no rolling graphite foil” reduces these differences to 50K.

Corrective factors were applied to model the drop in electrical and thermal contact resistances to correspond at the “no rolling graphite foil” configuration. These contact resistance data will be precious information for future models, and applications. For example in Flash-SPS or high heating rate tests where intense thermal confinement takes place because of the behavior of these contacts.

5. Acknowledgements

The authors thank the Normandy RIN Region Project DEFORMINT n°20191118181931000002100002257 for the financial support of this study and Christelle Bilot for the SEM image.

Data availability

[1] X. Wei, O. Izhvanov, C. Back, C.D. Haines, D.G. Martin, K.S. Vecchio, E.A. Olevsky, Spark plasma sintering of structure-tailored ultrahigh-temperature components: First step to complex net shaping, J. Am. Ceram. Soc. 102 (2018) 1–12. https://doi.org/10.1111/jace.15752.

[2] S.A. Ghaffari, M.A. Faghihi-Sani, F. Golestani-Fard, H. Mandal, Spark plasma sintering of TaC-HfC UHTC via disilicides sintering aids, J. Eur. Ceram. Soc. 33 (2013) 1479–1484. https://doi.org/10.1016/j.jeurceramsoc.2013.01.017.

[3] G.J. Zhang, W.M. Guo, D.W. Ni, Y.M. Kan, Ultrahigh temperature ceramics (UHTCs) based on ZrB2 and HfB2 systems: Powder synthesis, densification and mechanical properties, J. Phys. Conf. Ser. 176 (2009). https://doi.org/10.1088/1742-6596/176/1/012041.

[4] G. Jin, M. Takeuchi, S. Honda, T. Nishikawa, H. Awaji, Properties of multilayered mullite/Mo functionally graded materials fabricated by powder metallurgy processing, Mater. Chem. Phys. 89 (2005) 238–243. https://doi.org/10.1016/j.matchemphys.2004.03.031.

[5] H. Mishina, Y. Inumaru, K. Kaitoku, Fabrication of ZrO2/AISI316L functionally graded materials for joint prostheses, Mater. Sci. Eng. A. 475 (2008) 141–147. https://doi.org/10.1016/j.msea.2007.05.004.

[6] H. Guo, K.A. Khor, Y.C. Boey, X. Miao, Laminated and functionally graded hydroxyapatite/yttria stabilized tetragonal zirconia composites fabricated by spark plasma sintering, Biomaterials. 24 (2003) 667–675. https://doi.org/10.1016/S0142-9612(02)00381-2.

[7] S. Deng, R. Li, T. Yuan, P. Cao, Effect of electric current on crystal orientation and its contribution to densification during spark plasma sintering, Mater. Lett. 229 (2018) 126–129. https://doi.org/10.1016/j.matlet.2018.07.001.

[8] S. Seyyedin, H. Zangi, M. Bozorgmehr, B. Ghasemi, M.M. Tavallaei, S. Adib, The effect of mechanical alloying time on the microstructural and mechanical properties of spark plasma sintered Ta–10W, Mater. Sci. Eng. A. 798 (2020) 140024. https://doi.org/10.1016/j.msea.2020.140024.

[9] R. Ohser-Wiedemann, U. Martin, H.J. Seifert, A. Müller, Densification behaviour of pure molybdenum powder by spark plasma sintering, Int. J. Refract. Met. Hard Mater. 28 (2010) 550–557. https://doi.org/10.1016/j.ijrmhm.2010.03.003.

[10] Z. Tan, L. Wang, Y. Xue, G. Wang, Z. Zhou, L. Tian, Y. Wang, B. Wang, D. He, A multiple grain size distributed Al-based composite consist of amorphous/nanocrystalline, submicron grain and micron grain fabricated through spark plasma sintering, J. Alloys Compd. 737 (2018) 308–316. https://doi.org/10.1016/j.jallcom.2017.12.102.

[11] M. Algueró, T. Hungría, H. Amorín, J. Ricote, J. Galy, A. Castro, Relaxor behavior, polarization buildup, and switching in nanostructured 0.92PbZn1/3Nb2/3O3-0-08 PbTiO3 ceramics, Small. 3 (2007) 1906–1911. https://doi.org/10.1002/smll.200700284.

[12] M. Herrmann, Z. Shen, I. Schulz, J. Hu, B. Janear, Silicon nitride nanoceramics densified by dynamic grain sliding, J. Mater. Res. 25 (2010) 2354–2361. https://doi.org/10.1557/jmr.2010.0313.

[13] Y. Achenani, M. Saâdaoui, A. Cheddadi, G. Bonnefont, G. Fantozzi, Finite element modeling of spark plasma sintering: Application to the reduction of temperature inhomogeneities, case of alumina, Mater. Des. 116 (2017) 504–514. https://doi.org/10.1016/j.matdes.2016.12.054.

[14] R. Collet, S. Le Gallet, F. Charlot, S. Lay, J.-M. Chaix, F. Bernard, Effect of Electric Current on SPS Densification of Spherical Copper Powder, J. Manuf. Mater. Process. 5 (2021) 119. https://doi.org/10.3390/jmmp5040119.

[15] C. Manière, G. Lee, J. McKittrick, E.A. Olevsky, Energy efficient spark plasma sintering: Breaking the threshold of large dimension tooling energy consumption, J. Am.

Ceram. Soc. 102 (2019) 706–716. https://doi.org/10.1111/jace.16046.

[16] A. Zavaliangos, J. Zhang, M. Krammer, J.R. Groza, Temperature evolution during field activated sintering, Mater. Sci. Eng. A. 379 (2004) 218–228. https://doi.org/10.1016/j.msea.2004.01.052.

[17] U. Anselmi-Tamburini, J.E. Garay, Z.A. Munir, Fundamental investigations on the spark plasma sintering/synthesis process, Mater. Sci. Eng. A. 407 (2005) 24–30. https://doi.org/10.1016/j.msea.2005.06.066.

[18] O. Guillon, J. Gonzalez-Julian, B. Dargatz, T. Kessel, G. Schierning, J. Räthel, M. Herrmann, Field-assisted sintering technology/spark plasma sintering: Mechanisms, materials, and technology developments, Adv. Eng. Mater. 16 (2014) 830–849. https://doi.org/10.1002/adem.201300409.

[19] C. Manière, L. Durand, E. Brisson, H. Desplats, P. Carré, P. Rogeon, C. Estournès, Contact resistances in spark plasma sintering: From in-situ and ex-situ determinations to an extended model for the scale up of the process, J. Eur. Ceram. Soc. 37 (2017) 1593–1605. https://doi.org/10.1016/j.jeurceramsoc.2016.12.010.

[20] C. Arnaud, C. Manière, G. Chevallier, C. Estournès, R. Mainguy, F. Lecouturier, D. Mesguich, A. Weibel, L. Durand, C. Laurent, Dog-bone copper specimens prepared by one-step spark plasma sintering, J. Mater. Sci. 50 (2015) 7364–7373. https://doi.org/10.1007/s10853-015-9293-5.

[21] C. Manière, C. Harnois, G. Riquet, J. Lecourt, C. Bilot, S. Marinel, Flash spark plasma sintering of zirconia nanoparticles: Electro-thermal-mechanical-microstructural simulation and scalability solutions, J. Eur. Ceram. Soc. 42 (2022) 216–226. https://doi.org/10.1016/j.jeurceramsoc.2021.09.021.

[22] C. Manière, G. Lee, E.A. Olevsky, Flash sintering of complex shapes, Appl. Mater. Today. 26 (2022) 101293. https://doi.org/10.1016/j.apmt.2021.101293.

[23] C. Manière, G. Lee, E.A. Olevsky, All-Materials-Inclusive Flash Spark Plasma Sintering, Sci. Rep. 7 (2017) 15071. https://doi.org/10.1038/s41598-017-15365-x.

[24] D. Giuntini, E. Olevsky, C. Garcia-Cardona, A. Maximenko, M. Yurlova, C. Haines, D. Martin, D. Kapoor, Localized Overheating Phenomena and Optimization of Spark-Plasma Sintering Tooling Design, Materials (Basel). 6 (2013) 2612–2632. https://doi.org/10.3390/ma6072612.

[25] X. Wei, D. Giuntini, A.L. Maximenko, C.D. Haines, E.A. Olevsky, Experimental Investigation of Electric Contact Resistance in Spark Plasma Sintering Tooling Setup, J. Am. Ceram. Soc. 98 (2015) 3553–3560. https://doi.org/10.1111/jace.13621.

[26] G. Maizza, S. Grasso, Y. Sakka, Moving finite-element mesh model for aiding spark plasma sintering in current control mode of pure ultrafine WC powder, J. Mater. Sci. 44 (2009) 1219–1236. https://doi.org/10.1007/s10853-008-3179-8.

[27] C. Manière, L. Durand, A. Weibel, C. Estournès, Spark-plasma-sintering and finite element method: From the identification of the sintering parameters of a submicronic α-alumina powder to the development of complex shapes, Acta Mater. 102 (2016) 169–175. https://doi.org/10.1016/j.actamat.2015.09.003.

[28] C. Wang, L. Cheng, Z. Zhao, FEM analysis of the temperature and stress distribution in spark plasma sintering: Modelling and experimental validation, Comput. Mater. Sci. 49 (2010) 351–362. https://doi.org/10.1016/j.commatsci.2010.05.021.

[29] C. Maniere, A. Pavia, L. Durand, G. Chevallier, V. Bley, K. Afanga, A. Peigney, C. Estournès, Pulse analysis and electric contact measurements in spark plasma sintering, Electr. Power Syst. Res. 127 (2015) 307–313. https://doi.org/10.1016/j.epsr.2015.06.009.

[30] A. Van der Laan, V. Boyer, R. Epherre, C. Estournès, Simple method for the identification of electrical and thermal contact resistances in spark plasma sintering, J. Eur. Ceram. Soc. 41 (2021) 599–610. https://doi.org/10.1016/j.jeurceramsoc.2020.08.073.

[31] U. Anselmi-Tamburini, S. Gennari, J.E. Garay, Z.A. Munir, Fundamental investigations on the spark plasma sintering/synthesis process: II. Modeling of current and temperature

distributions, Mater. Sci. Eng. A. 394 (2005) 139–148. https://doi.org/10.1016/j.msea.2004.11.019.

[32] C. Maniere, A. Pavia, L. Durand, G. Chevallier, V. Bley, K. Afanga, A. Peigney, C. Estournès, Pulse analysis and electric contact measurements in spark plasma sintering, Electr. Power Syst. Res. 127 (2015) 307–313. https://doi.org/10.1016/j.epsr.2015.06.009.

[33] M.M. Yovanovich, Four decades of research on thermal contact, gap, and joint resistance in microelectronics, IEEE Trans. Components Packag. Technol. 28 (2005) 182–206. https://doi.org/10.1109/TCAPT.2005.848483.

[34] C. Manière, A. Pavia, L. Durand, G. Chevallier, K. Afanga, C. Estournès, Finite-element modeling of the electro-thermal contacts in the spark plasma sintering process, J. Eur. Ceram. Soc. 36 (2016) 741–748. https://doi.org/10.1016/j.jeurceramsoc.2015.10.033.